

Magnetic Excitation Spectra in BaFe₂As₂: A Two-Particle Approach within a Combination of the Density Functional Theory and the Dynamical Mean-Field Theory Method

Hyowon Park, Kristjan Haule, and Gabriel Kotliar

Department of Physics, Rutgers University, Piscataway, New Jersey 08854, USA

(Received 14 April 2011; published 23 September 2011)

We study the magnetic excitation spectra in the paramagnetic state of BaFe₂As₂ from the *ab initio* perspective. Both the one-particle and the magnetic two-particle excitation spectra are determined within the combination of the density functional theory and the dynamical mean-field theory method. This method reproduces all the experimentally observed features in inelastic neutron scattering and relates them to both the one-particle excitations and the collective modes. The magnetic excitation dispersion is well accounted for by our theoretical calculation in the paramagnetic state without any broken symmetry; hence, nematic order is not needed to explain the inelastic neutron scattering experimental data.

DOI: 10.1103/PhysRevLett.107.137007

PACS numbers: 74.70.Xa, 71.27.+a, 75.40.Gb

Neutron scattering experiments provide strong constraints on the theory of iron pnictides. Both the localized picture and the itinerant picture of the magnetic response have had some successes in accounting for or even predicting aspects of the experiments. Calculations based on a spin model with frustrated exchange constants [1,2] or with biquadratic interactions [3] described well the neutron scattering experiments [4,5]. The itinerant magnetic model, based on a random phase approximation form of the magnetic response [6–9], produces equally good descriptions of the experimental data. Density functional theory (DFT) calculations predicted the stripe nature of the ordering pattern [10] and the anisotropic values of the exchange constants in the magnetic phase [11]. The tight binding calculations based on DFT bands also predicted the existence of a resonance mode in the superconducting state [12].

In spite of these successes, both itinerant and localized models require significant extensions to fully describe the experimental results. DFT fails to predict the observed ordered moment [11]. Furthermore, adjusting parameters such as the arsenic height to reproduce the ordered moment leads to a peak in the density of states at the Fermi level [6] instead of the pseudogap, which is observed experimentally. The localized picture cannot describe the magnetic order in the FeTe material without introducing additional longer range exchange constants. Furthermore, fits of the inelastic neutron scattering (INS) data require the use of anisotropic exchange constants well above the magnetic ordering temperature [13]. However, no clear phase transition to a nematic phase in this range has been detected.

In this Letter, we show that the combination of density functional theory and dynamical mean-field theory (DFT + DMFT) provides a natural way to improve both the localized and the itinerant picture and connects the neutron response to structural material specific information and to the results of other spectroscopies. The DFT + DMFT method has been previously used to compute the local dynamical [14,15] and the uniform static magnetic

susceptibility [16] in Fe pnictides. The dynamic susceptibility for all momenta and frequency, which requires calculation of the two-particle vertex, is done here for the first time.

We compute the one-particle Green's function by using the charge self-consistent full potential DFT + DMFT method, as implemented in Ref. [17], based on the WIEN2K code [18]. We used continuous-time quantum Monte Carlo calculations [19,20] as the quantum impurity solver and the Coulomb interaction matrix as determined in Ref. [21]. The dynamical magnetic susceptibility $\chi(\mathbf{q}, \omega)$ is computed from the *ab initio* perspective by extracting the two-particle vertex functions of DFT + DMFT solution $\Gamma_{\text{loc}}^{\text{irr}}$ [22]. The polarization bubble χ^0 is computed from the fully interacting one-particle Green's function. The full susceptibility is computed from χ^0 and the two-particle irreducible vertex function $\Gamma_{\text{loc}}^{\text{irr}}$, which is assumed to be local in the same basis in which the DMFT self-energy is local, implemented here by the projector to the muffin-tin sphere [17]. In order to extract $\Gamma_{\text{loc}}^{\text{irr}}$, we employ the Bethe-Salpeter equation (see Fig. 1), which relates the local two-particle Green's function (χ_{loc}), sampled by continuous-time quantum Monte Carlo calculations, with both the local polarization function (χ_{loc}^0) and $\Gamma_{\text{loc}}^{\text{irr}}$:

$$\Gamma_{\text{loc}}^{\text{irr}}{}_{\alpha_3\sigma_3, \alpha_4\sigma_4}^{\alpha_1\sigma_1, \alpha_2\sigma_2}(i\nu, i\nu')_{i\omega} = \frac{1}{T} [(\chi_{\text{loc}}^0)_{i\omega}^{-1} - \chi_{\text{loc}}^{-1}]. \quad (1)$$

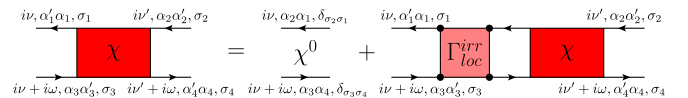


FIG. 1 (color online). The Feynman diagrams for the Bethe-Salpeter equation. It relates the two-particle Green's function (χ) with the polarization (χ^0) and the local irreducible vertex function ($\Gamma_{\text{loc}}^{\text{irr}}$). The nonlocal two-particle Green's function is obtained by replacing the local propagator by the nonlocal propagator.

$\Gamma_{\text{loc}}^{\text{irr}}$ depends on three Matsubara frequencies ($i\nu$, $i\nu'$, and $i\omega$), and both the spin (σ_{1-4}) and the orbital (α_{1-4}) indices, which run over $3d$ states on the iron atom. T is the temperature.

Once the irreducible vertex $\Gamma_{\text{loc}}^{\text{irr}}$ is obtained, the momentum-dependent two-particle Green's function is constructed again by using the Bethe-Salpeter equation (Fig. 1) by replacing the local polarization function χ_{loc}^0 by the nonlocal one $\chi_{\mathbf{q},i\omega}^0$:

$$\chi_{\alpha_3\sigma_3,\alpha_4\sigma_4}^{\alpha_1\sigma_1,\alpha_2\sigma_2}(i\nu, i\nu')_{\mathbf{q},i\omega} = [(\chi^0)_{\mathbf{q},i\omega}^{-1} - T\Gamma_{\text{loc}}^{\text{irr}}]^{-1}. \quad (2)$$

Finally, the dynamic magnetic susceptibility $\chi(\mathbf{q}, i\omega)$ is obtained by closing the two-particle Green's function with the magnetic moment $\boldsymbol{\mu} = \mu_B(\mathbf{L} + 2\mathbf{S})$ vertex and summing over frequencies ($i\nu$ and $i\nu'$), orbitals (α_{1-4}), and spins (σ_{1-4}) on the four external legs:

$$\chi(\mathbf{q}, i\omega) = T \sum_{i\nu, i\nu'} \sum_{\substack{\alpha_1\sigma_1 \\ \alpha_3\sigma_3}} \sum_{\substack{\alpha_2\sigma_2 \\ \alpha_4\sigma_4}} \mu_{\alpha_1\sigma_1}^z \mu_{\alpha_2\sigma_2}^z \chi_{\alpha_3\sigma_3,\alpha_4\sigma_4}^{\alpha_1\sigma_1,\alpha_2\sigma_2}(i\nu, i\nu')_{\mathbf{q},i\omega}. \quad (3)$$

The resulting dynamical magnetic susceptibility is obtained in Matsubara frequency ($i\omega$) space, and it needs to be analytically continued to real frequencies [$\chi(\mathbf{q}, \omega)$]. For the low frequency region, on which we concentrate here, the vertex $\Gamma_{\text{loc}}^{\text{irr}}$ is analytically continued by a quasiparticle-like approximation. We replace the frequency-dependent vertex with a constant, i.e., $\Gamma_{\text{loc}}^{\text{irr}, \alpha_1\sigma_1,\alpha_2\sigma_2}(i\nu, i\nu')_{i\omega} \approx \bar{U}_{\alpha_3\sigma_3,\alpha_4\sigma_4}^{\alpha_1\sigma_1,\alpha_2\sigma_2}$, and require $\chi(\mathbf{q}, i\omega = 0) = \chi(\mathbf{q}, \omega = 0)$. This vertex \bar{U} , however, retains important spin and orbital dependence.

Figure 2(a) shows the calculated constant energy plot of the dynamical structure factor $S(\mathbf{q}, \omega)$ in the paramagnetic state of BaFe_2As_2 . Our theoretical results are calculated in the unfolded Brillouin zone of one Fe atom per unit cell, because magnetic excitations are concentrated primarily on Fe atoms; therefore, folding, which occurs due to the two inequivalent arsenic atoms in the unit cell, is not noticeable in the magnetic response [7]. For comparison, we also reproduce in Fig. 2(b) the INS experimental data from Ref. [13]. At low energy (around $\omega = 50$ meV), the theoretical $S(\mathbf{q}, \omega)$ is strongly peaked at the ordering wave vector $(H, K, L) = (1, 0, 1)$, and it forms a clear elliptical shape elongated in the K direction. The elongation of the ellipse increases with energy ($\omega = 75$ meV), and around $\omega = 125$ meV the ellipse splits into two peaks, one peak centered at $(1, 0.4, 1)$ and the other at $(1, -0.4, 1)$. At even higher energy ($\omega \approx 150$ meV), the magnetic spectra broaden, and peaks from four equivalent wave vectors merge into a circular shape centered at wave vector $(1, 1, 1)$. At even higher energy (230 meV, not shown in the figure), the spectra broaden further, and the peak becomes centered at the point $(1, 1, 1)$. These trends are all in good quantitative agreement with INS data from Fig. 2(b).

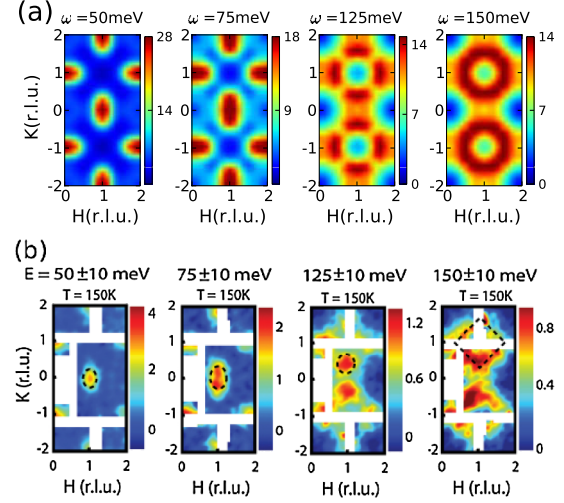


FIG. 2 (color online). (a) The constant energy plot of the theoretical dynamical structure factor $S(\mathbf{q}, \omega)$ ($= \frac{\chi''(\mathbf{q}, \omega)}{1 - e^{-\hbar\omega/k_B T}}$) at different energies (50, 75, 125, and 150 meV) in the paramagnetic state ($T = 386$ K) of BaFe_2As_2 as a function of momentum $\mathbf{q} = (H, K, L)$. L is here fixed at 1. (b) The corresponding inelastic neutron scattering data from Ref. [13].

Figure 3 displays a contour plot of the theoretical $S(\mathbf{q}, \omega)$ as a function of frequency ω and momentum \mathbf{q} . At low energies ($\omega < 80$ meV), $S(\mathbf{q}, \omega)$ is mostly concentrated in the region near the ordering vector $(1, 0, 1)$. Consistent with the elongation of the ellipse along the K direction in Fig. 2, the low energy ($\omega < 80$ meV) bright spot in Fig. 3 is extended further towards the $(1, 1, 1)$ direction but quite abruptly decreases in the $(0, 0, 1)$ direction. The magnetic spectra in the two directions $(1, 0, 1) \rightarrow (0, 0, 1)$ and $(1, 0, 1) \rightarrow (1, 1, 1)$ are clearly different even at higher energy $\omega > 100$ meV. The peak position is moving to higher energy along both paths, but it fades away very

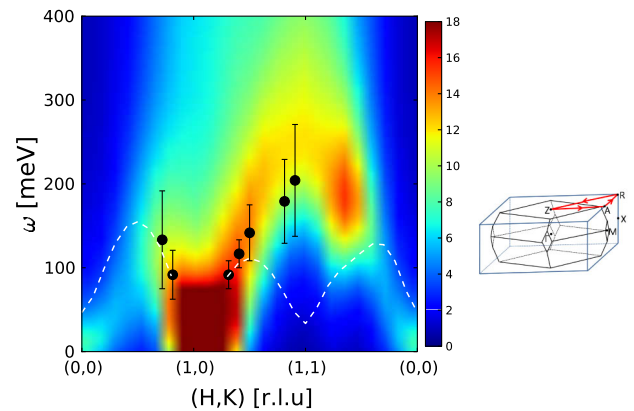


FIG. 3 (color online). $S(\mathbf{q}, \omega)$ along the special path in the Brillouin zone marked by a red arrow in the inset on the right. The inset shows the body-centered tetragonal (black line) and the unfolded (blue line) Brillouin zone. Black dots with error bars correspond to INS data from Ref. [13]. The white dashed line shows the isotropic Heisenberg spin wave dispersion.

quickly along the first path, such that the signal practically disappears at $(0.5, 0, 1)$. Along the second path $(1, 0, 1) \rightarrow (1, 1, 1)$, there remains a well-defined excitation peak for which the energy is increasing and at $(1, 1, 1)$ reaches the maximum value of ≈ 230 meV. Continuing the path from $(1, 1, 1)$ towards $(0, 0, 1)$, the peak energy decreases again, and it fades away around $(0.5, 0.5, 1)$. The black dots display INS data with error bars from Ref. [13]. Notice a very good agreement between theory and experiment.

The white dashed line in Fig. 3 represents the spin wave dispersion obtained for the isotropic Heisenberg model using nearest neighbor J_1 and next nearest neighbor J_2 exchange constants and performing the best fit to INS data. This fit was performed in Ref. [13]. The magnetic excitation spectra of an isotropic Heisenberg model show a local minimum at the wave vector $\mathbf{q} = (1, 1, 1)$, which is inconsistent with our theory and with the experiment. To better fit the experimental data with a Heisenberg-like model, very anisotropic exchange constants need to be assumed [13], which raised speculations about the possible existence of a nematic phase well above the structural transition of BaFe_2As_2 . Since the DFT + DMFT results can account for all the features of the measured magnetic spectra without invoking any rotationally symmetry breaking, the presence of nematicity in the paramagnetic tetragonal state at high temperature is unlikely, as also pointed out by Ref. [7].

In Fig. 4(a), we show constant frequency cuts in the K direction [from $(1, -1, 1)$ through $(1, 0, 0)$ to $(1, 1, 1)$] of $S(\mathbf{q}, \omega)$ displayed in Fig. 3. For comparison, we also show the corresponding INS measurements from Ref. [13] as red circles in Figs. 4(b) and 4(c). At $\omega = 20$ meV, the spectrum

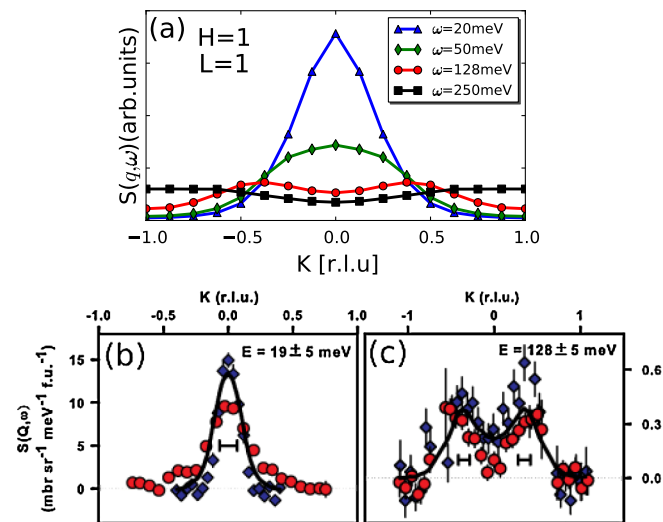


FIG. 4 (color online). (a) The wave vector K dependence ($H = 1, L = 1$) of $S(\mathbf{q}, \omega)$ at several frequencies. (b) The corresponding INS data at $\omega = 19$ and (c) 128 meV reproduced from Ref. [13]. The red circles correspond to the paramagnetic state at $T = 150$ K and the blue diamonds to the magnetic state at $T = 7$ K.

has a sharp peak centered at the ordering vector $(1, 0, 1)$. At $\omega = 50$ meV, the spectrum still displays a peak at $(1, 0, 1)$, but the intensity is significantly reduced. With increasing frequency ω , the peak position in $S(\mathbf{q}, \omega)$ moves in the direction of $(1, 1, 1)$ and at 128 meV peaks around $(1, 0.4, 1)$. The shift of the peak is accompanied with substantial reduction of intensity at ordering wave vector $(1, 0, 1)$. At even higher energy of 250 meV, only a very weak peak remains, and it is centered at the wave vector $(1, 1, 1)$. The position of peaks as well as their frequency dependence is in very good agreement with INS experiments of Ref. [13] displayed in Figs. 4(b) and 4(c).

Figure 5(a) resolves the dynamical magnetic susceptibility χ of Eq. (3) in the orbital space $\chi_\alpha = T \sum_{i\nu, i\nu'} \sum_\beta \sum_{\sigma_3 \sigma_4} \mu_{\sigma_1 \sigma_3}^z \mu_{\sigma_2 \sigma_4}^z \chi_{\alpha\sigma_1, \beta\sigma_2}^{\alpha\sigma_3, \beta\sigma_4}(i\nu, i\nu')$ such that $\chi = \sum_\alpha \chi_\alpha$. At the magnetic ordering vector $\mathbf{q} = (1, 0, 1)$, χ''_α increases sharply with frequency near $\omega = 0$ for all orbitals and is strongly suppressed above 100 meV, reaching the maximum around 20 meV. At this wave vector, the dominant contributions at low energy come from the d_{xy} and the d_{yz} orbitals. The magnetic susceptibility at $\mathbf{q} = (0, 1, 1)$ in Fig. 5(a) shows the same trend as orbitally resolved spectra at $\mathbf{q} = (1, 0, 1)$ except that d_{xz} and d_{yz} switch their roles due to the C_4 symmetry of the Fe square lattice.

These dominant orbital contributions to χ are also reasonably captured in the polarization bubble χ^0 (not shown here); hence, these excitations could be understood in terms of the Fermi surface nesting. The orbitally resolved Fermi surface is displayed in Fig. 5(b) at both the Γ plane and the Z plane. Most of the weight in χ^0 comes from the diagonal terms, i.e., $\chi_{\alpha, \alpha}^0$; hence, the Fermi surfaces with the same color in Fig. 5(b) but separated by the wave vector $(1, 0, 1)$ give a dominant contribution. The intraorbital d_{yz} low energy spectra come mostly from the transitions between the green parts of the hole pocket at Γ and the green parts of the electron pocket at A , marked with green squares (\square) in Fig. 5(b). Since the electron pocket at A is elongated in the H direction, the nesting condition occurs mostly in the perpendicular K direction; hence, the elliptical excitations at low energy in Fig. 2 are elongated in the K but not in the H direction. The intraorbital d_{xy} transitions are pronounced between the electron pocket at M' and the hole pocket at R , as well as between the electron pocket at A' and the hole pocket at X (marked with red \circ). This large spin response at $(1, 0, 1)$ gives rise to the low energy peak in Fig. 3.

We note that the particle-hole response, encoded in polarization bubble χ^0 , is especially large when nesting occurs between an electron pocket and a hole pocket, because the nesting condition extends to the finite frequency, and is not cut off by the Fermi functions.

The low energy magnetic excitations at wave vectors $\mathbf{q} = (0, 0, 1)$ and $\mathbf{q} = (1, 1, 1)$ can come only from electron-electron or hole-hole transitions; hence, both

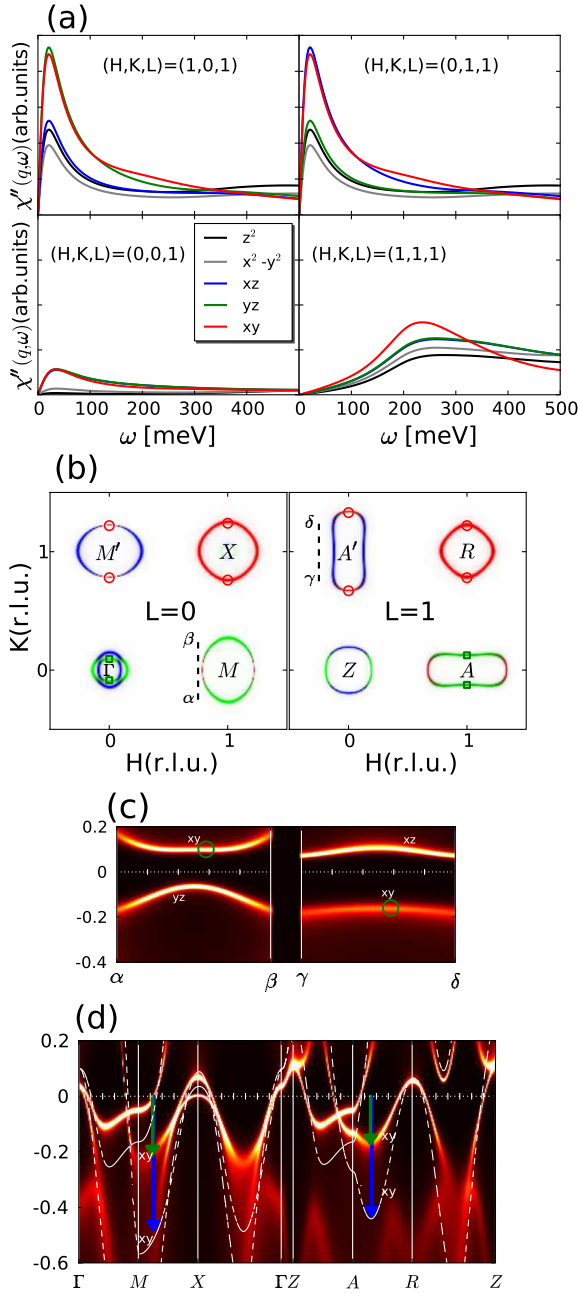


FIG. 5 (color online). (a) The Fe d orbital resolved dynamical magnetic susceptibility at $T = 386$ K for distinct wave vectors $\mathbf{q} = (1, 0, 1)$, $(0, 1, 1)$, $(0, 0, 1)$, and $(1, 1, 1)$. Different colors correspond to different orbital contributions. (b) The Fermi surface in the Γ and Z plane at $T = 73$ K colored by the orbital characters: d_{xz} (blue), d_{yz} (green), and d_{xy} (red). The small symbols mark the regions in the Fermi surface, where nesting for the wave vector $\mathbf{q} = (1, 0, 1)$ is good. (c) The zoom-in of $A(\mathbf{k}, \omega)$ along the path marked by a black dashed line in (b). The green open circles indicate the two relevant bands of d_{xy} character which give rise to the peak in magnetic excitation spectra near 230 meV at $\mathbf{q} = (1, 1, 1)$. (d) $A(\mathbf{k}, \omega)$ computed in one Fe atom per unit cell at $T = 73$ K. The green arrows mark the same bands which give rise to the 230 meV peak. The DFT bands are overlaid by white dashed lines. The blue arrows mark corresponding DFT bands of d_{xy} character.

responses are quite small, as seen in Fig. 5(a). While the magnetic response at $\mathbf{q} = (0, 0, 1)$ is small but finite, the spin response at $\mathbf{q} = (1, 1, 1)$ is almost gapped. This is because the hole-hole transitions from Γ to R or electron-electron transitions from M to A' do not involve any intra-orbital transitions and, hence, are even smaller than transitions at the wave vector $(0, 0, 1)$.

At finite energy transfer, the spin excitations come from electronic states away from the Fermi energy and cannot be easily identified in the Fermi surface plot. Hence, it is more intriguing to find the dominant contribution to the peak at $\omega \approx 230$ meV and $\mathbf{q} = (1, 1, 1)$. This peak gives rise to the 230 meV excitations at $(1, 1, 1)$ in Fig. 3. A large contribution to this finite frequency excitation comes from a region near the two electron pockets at M and A' marked with a black dashed line in Fig. 5(b). We display in Fig. 5(c) the one-electron spectral function across these dashed lines in the Brillouin zone to show an important particle-hole transition from the electrons above the Fermi level at the M point and the flat band at -200 meV around the A' point, both of d_{xy} character. We note that, due to large off-diagonal terms in the two-particle vertex Γ , all orbital contributions to χ develop a peak at the same energy, although only the d_{xy} orbital displays a pronounced peak in χ^0 .

Figure 5(d) displays the one-electron spectral function in a path through the Brillouin zone, corresponding to one Fe atom per unit cell [23]. Within DFT + DMFT the quasi-particle bands are renormalized by a factor of 2–3 compared to the corresponding DFT bands (white dashed lines). The green arrow marks the d_{xy} band, which contributes to the peak in $S(\mathbf{q}, \omega)$ near 230 meV and $\mathbf{q} = (1, 1, 1)$. In the DFT calculation, this d_{xy} intraorbital transition is also present but occurs at a much higher energy of the order of 400–600 meV, marked by blue arrows. The overestimation of the peak energy at $\mathbf{q} = (1, 1, 1)$ was reported in the local spin density approximation calculation of Ref. [6].

In this Letter, we have extended the DFT + DMFT methodology to compute the two particle responses in a realistic multi-orbital DFT + DMFT setting. With the same parameters which were used to successfully describe the optical spectra and the magnetic moments of this material [24], we obtained a coherent description of the experimental neutron scattering results. Our theory ties the magnetic response to the fermiology of the model and quantifies the departure from both purely itinerant and localized pictures.

This research was supported by the National Science Foundation through Grants No. TG-DMR100048, No. NSF-DMR 0746395 (H. P. and K. H.), and No. NSF-DMR 0906943 (G. K.).

-
- [1] P. Goswami, R. Yu, Q. Si, and E. Abrahams, [arXiv:1009.1111](https://arxiv.org/abs/1009.1111).
 [2] R. Applegate, J. Oitmaa, and R. R. P. Singh, *Phys. Rev. B* **81**, 024505 (2010).

- [3] A. L. Wysocki, K. D. Belashchenko, and V. P. Antropov, *Nature Phys.* **7**, 485 (2011).
- [4] S. O. Diallo *et al.*, *Phys. Rev. Lett.* **102**, 187206 (2009).
- [5] J. Zhao *et al.*, *Nature Phys.* **5**, 555 (2009).
- [6] L. Ke, M. van Schilfgaarde, J. Pulikkotil, T. Kotani, and V. Antropov, *Phys. Rev. B* **83**, 060404 (2011).
- [7] J. T. Park *et al.*, *Phys. Rev. B* **82**, 134503 (2010).
- [8] S. Graser *et al.*, *Phys. Rev. B* **81**, 214503 (2010).
- [9] E. Kaneshita and T. Tohyama, *Phys. Rev. B* **82**, 094441 (2010).
- [10] J. Dong *et al.*, *Europhys. Lett.* **83**, 27006 (2008).
- [11] M. J. Han, Q. Yin, W. E. Pickett, and S. Y. Savrasov, *Phys. Rev. Lett.* **102**, 107003 (2009).
- [12] T. A. Maier, S. Graser, D. J. Scalapino, and P. Hirschfeld, *Phys. Rev. B* **79**, 134520 (2009).
- [13] L. W. Harriger *et al.*, *Phys. Rev. B* **84**, 054544 (2011).
- [14] P. Hansmann *et al.*, *Phys. Rev. Lett.* **104**, 197002 (2010).
- [15] K. Haule and G. Kotliar, *New J. Phys.* **11**, 025021 (2009).
- [16] S. L. Skornyakov, A. A. Katanin, and V. I. Anisimov, *Phys. Rev. Lett.* **106**, 047007 (2011).
- [17] K. Haule, C.-H. Yee, and K. Kim, *Phys. Rev. B* **81**, 195107 (2010).
- [18] P. Blaha *et al.*, *Wien2K* (Karlheinz Schwarz, Technische Universität Wien, Austria, 2001).
- [19] K. Haule, *Phys. Rev. B* **75**, 155113 (2007).
- [20] P. Werner, A. Comanac, L. de' Medici, M. Troyer, and A. J. Millis, *Phys. Rev. Lett.* **97**, 076405 (2006).
- [21] A. Kutepov, K. Haule, S. Y. Savrasov, and G. Kotliar, *Phys. Rev. B* **82**, 045105 (2010).
- [22] M. Jarrell, *Phys. Rev. Lett.* **69**, 168 (1992).
- [23] See Supplemental Material at <http://link.aps.org/supplemental/10.1103/PhysRevLett.107.137007> for the explanation of calculating a coherence factor at each band and each momentum point. This coherence factor is referred as “a projector to the unfolded (large) Brillouin zone” in the Supplemental Material.
- [24] Z. P. Yin, K. Haule, and G. Kotliar, *Nature Phys.* **7**, 294 (2011).